(Received 1 November 2024, Accepted 30 December 2024, Scheduled 5 February 2025)

Multi-Objective Optimization Design of a Bilayer Segmented Asymmetric Interior Permanent Magnet Synchronous Motor

Luyao Wang[1], Hui Zhu[2,*], Yunpeng Song[1], Wenjing Hu[1], Huihui Geng[1], Xueyi Zhang[1], Qi Yu[1], Xin Zhou[1], and Xingxu Jin[1]

[1] *College of Transportation and Vehicle Engineering, Shandong University of Technology, Zibo 255000, China*
[2] *School of engineering, Shandong Union College, Jinnan 250000, China*

ABSTRACT: This paper proposes a bilayer segmented asymmetric V-type magnetic structure of interior permanent magnet motor to address the problems of large air-gap magnetic density zero region, high air-gap magnetic density distortion rate, and large output torque ripple in the traditional V-type permanent magnet synchronous motor. Firstly, the superiority of the bilayer segmented asymmetric V-type structure is verified using finite element simulation compared with the bilayer conventional V-type and bilayer segmented symmetric V-type structures. Secondly, the analytical model of the air-gap magnetic density, output torque, and torque ripple is established. Then, with the optimization objectives of reducing the air-gap magnetic density distortion rate, increasing the output torque, and reducing the torque ripple, and with pole-span angles of the bilayer segmented asymmetric V-type structure as the optimization variables, each optimization variable is subjected to weighted sensitivity stratification. The response surface optimization is applied to the low- and medium-level sensitivity optimization variables, while a Pareto frontier distribution is used to obtain the set of the effective values of the high-level sensitivity optimization variables. The optional combination of the pole-span angles of the segmented asymmetric V-type structure is objectively selected by applying the TOPSIS method. Finally, the effectiveness of the optimized design is verified by finite element simulation and prototype tests. The results show that the bilayer segmented asymmetric V-type structure can reduce the percentage of the zero region of the air-gap from 4.82% to 3.91%, which is reduced by 18.8%, and lower the air-gap magnetic density distortion rate from 0.263 to 0.226, which is reduced by 14.1% while ensuring good output characteristics with improving the average output torque from 14.842 N·m to 16.418 N·m, which is increased by 10.6%, and reducing the torque ripple from 0.169 to 0.156, which is reduced by 7.7%.

1. INTRODUCTION

Interior V-type permanent magnet synchronous motors are widely used in electric vehicles due to superior advantages such as high power density and high efficiency [1–3]. However, due to the special V-type permanent magnet arrangement, the air-gap magnetization waveform has a certain zero region between the N-pole and S-pole. It affects the sinusoidality of the air-gap density, which in turn affects the motor's output torque and torque ripple [4–6]. Therefore, how to reduce the air-gap magnetic density distortion rate while ensuring the output performance, such as increasing the motor output torque and reducing the torque ripple, has become a hot issue for permanent magnet synchronous motors [7–9].

Scholars for permanent magnet synchronous motors to improve the sinusoidality of the air-gap magnetic density are mainly to improve the shape of the magnetic poles and change the eccentricity distance. Ref. [10] investigated the effect of different pole shapes on air-gap magnetic field harmonics. It proposed that segmented main and secondary poles can reduce the air-gap magnetic field and reaction potential harmonics. Still, it did not consider the existence of the zero region of the air gap, which affects the smoothness of the motor. Ref. [11] also proposed using a split permanent magnet instead of a single permanent magnet. The pole arc coefficient and eccentricity distance were selected as the optimization parameters, which achieves the goal of eliminating the magnetic field harmonics of the specified order so that the harmonic component of the air gap magnetic field is reduced, which likewise complicates the processing of the permanent magnets and the spatial arrangement of the rotor. Ref. [12] investigated the relationship between the pole eccentricity and the air-gap magnetic density distortion rate of permanent magnet motors and used finite element simulation to derive the optimal pole eccentricity but only optimized a certain pole parameter and did not consider the influence of other factors.

The research for permanent magnet synchronous motor torque ripple suppression is mostly based on rotor structural improvement. Ref. [13] biased the upper and lower two rotors based on a traditional V-type structure in the opposite direction. This structure can obtain a larger output torque but for the upper and lower two rotors of the installation of high precision requirements, such as if the positioning is inaccurate to increase the output torque ripple in turn. Refs. [14, 15] using an asymmetric structure can cancel the odd harmonics in the rotor magnetic dynamic potential, thus suppressing the torque ripple. But to a certain extent, it weakened the average output torque of the motor. Ref. [16] proposed a 1.5-layer permanent magnet structure with an asymmetric arrangement of the

* Corresponding author: Hui Zhu (zhuhui@sdxiehe.edu.cn).

V-shape PMs and spoke PMs, together with an asymmetric flux barrier located near the rotor surface in each pole. This structure had a larger output torque than the traditional V-type structure. However, it had a large region of the "zero zone" of the air-gap magnetization. Ref. [17] proposed a novel asymmetric delta-type and spoke-type interior permanent magnet synchronous machine, which used the magnetic field shifting technique to maximise the average torque and lessen torque ripples. However, it leaded to permanent magnet losses through eddy currents and subsequent overheating. Ref. [18] proposed an interior permanent magnet machine with asymmetrical configuration, which can have a magnet axis shifted effect. It exhibited a noticeable enhancement. However, it also had a very complicated structural design. Ref. [19] proposed a segmented magnet permanent magnet synchronous motor, and the sum of the widths of the two magnets in the segmented V-type magnet structure is larger than the width of the conventional V-type magnets. Therefore, the average output torque of the segmented V-type magnet structure is also larger. Still, there are more odd harmonics in the magnetic potential of the rotor of the segmented V-type structure, which results in a larger torque ripple of the structure.

Aiming at the above existing problems, this paper proposes a bilayer segmented asymmetric V-type magnetic pole structure based on a conventional V-type structure and segmented symmetric structure, which can reduce the percentage of the zero region of the air-gap and lower the air-gap magnetic density distortion rate while ensuring good output characteristics with improving the average output torque and reducing the torque ripple. The main innovations of this paper are shown below:

(1) A bilayer segmented asymmetric structure is proposed, which is divided into upper and lower layers of V-type magnets, and the upper and lower layers of magnets are decomposed into proximal and distal ends, respectively, with unequal angles between the upper and lower layers of magnets and unequal angles between the N-pole and S-pole at the same time. This structure can reduce the generation of the air gap zero region and air gap magnet distortion rate, and at the same time ensure the output torque and reduce the torque ripple.

(2) An analytical model of the air-gap magnetic field for this bilayer segmented asymmetric V-type structure is proposed based on the subdomain method, aiming at solving the problem that asymmetric structures are difficult to be modelled, and the model has a high computational accuracy.

(3) The weighted sensitivity analysis method is proposed; the sensitivity of different optimization objectives is considered comprehensively; and the design variables are classified into low-level sensitivity, medium-level sensitivity, and high-level sensitivity parameters, which reduce the amount of computation, aiming to solve the problem of the complex design process and low accuracy.

The rest of the paper is structured as follows. Section 2 establishes a bilayer segmented asymmetric topology model and preliminarily determines the values of each parameter and compares the performance of air-gap density distortion rate, output torque, and torque ripple of bilayer conventional V-type structure, bilayer segmented symmetric V-type structure, and bilayer segmented asymmetric V-type structure, to validate the correctness and superiority of the structure. Section 3 establishes the analytical model of the bilayer segmented asymmetric V-type structure based on the subdomain method and verifies the correctness and accuracy of the analytical model establishment by the finite element method. Section 4 analyzes the relationship between the design variables and optimization objective, and optimizes the optimization variables in a hierarchy according to weighted sensitivity. Section 5 verifies the performance of the optimized bilayer segmented asymmetric V-type structure using finite element analysis method and prototype test respectively to prove the validity and accuracy of this study. Section 6 gives the conclusion of this paper.

2. SPECIFIC STRUCTURE PROPOSED

2.1. Structure

This paper proposes a bilayer segmented asymmetric V-type structure, which is divided into two layers of upper and lower V-type magnets, and each layer of magnets is divided into proximal and distal ends, while the angles of the upper and lower layers of magnets are not equal, and the angle of the N-pole is not equal to the angle of the S-pole. The specific structure is as follows:

In the first layer of magnetic poles, the conventional V-type magnetic poles are decomposed into the first permanent magnet on the near air gap side and the second permanent magnet on the near rotating axis side. The angle a of the first permanent magnet of the N-pole and the angle e of the first permanent magnet of the S-pole are unequal, i.e., $a - e \neq 0$. The angle b of the second permanent magnet of the N-pole and the angle g of the second permanent magnet of the S-pole are unequal, i.e., $b - g \neq 0$. Similarly, in the second layer of magnetic poles, the conventional V-type magnetic poles are decomposed into the third permanent magnet on the near air gap side and the fourth permanent magnet on the near rotor axis side. The angle c of the third permanent magnet of the N-pole and the angle h of the third permanent magnet of the S-pole are unequal, i.e., $c - h \neq 0$. The angle d of the fourth permanent magnet of the N-pole and the angle j of the fourth permanent magnet of the S-pole are unequal, i.e., $d - j \neq 0$.

This structure can suppress the generation of the "zero zone" of the air-gap magnetization. At the same time, due to the existence of bilayer magnets, the magnetic leakage of this structure is reduced compared with traditional V-type structure, so this structure has higher power density and larger output torque. Due to the asymmetry of the pole span angle between the N-pole and the S-pole, the high harmonics in the air gap magnetization can be reduced, which in turn reduces the output torque ripple. The specific structure is shown in Fig. 1.

The main parameters of the motor are shown in Table 1.

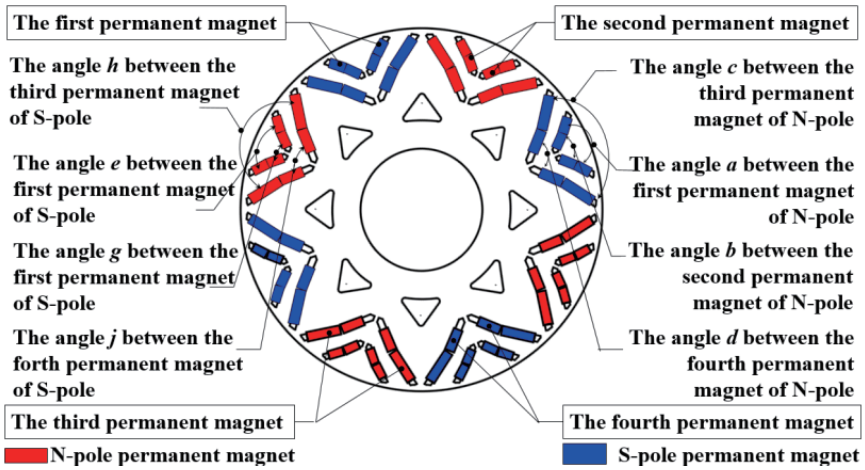

FIGURE 1. Schematic rotor structure of bilayer segmented asymmetric V-type permanent magnet synchronous motor.

TABLE 1. Main parameters of the motor.

Parameter	Value	Unit
Rated power	5	kW
Rated speed	3000	$r \cdot min^{-1}$
Rated voltage	72	V
Number of poles	8	
Number of slots	36	
The width of the first permanent magnet	2.8	mm
The length of the first permanent magnet	5	mm
The width of the second permanent magnet	2.8	mm
The length of the second permanent magnet	5	mm
The width of the third permanent magnet	3	mm
The length of the third permanent magnet	11	mm
The width of the fourth permanent magnet	3	mm
The length of the fourth permanent magnet	9.6	mm
The angle a between the first permanent magnet of N-pole	104	°
The angle b between the second permanent magnet of N-pole	91	°
The angle c between the third permanent magnet of N-pole	106	°
The angle d between the fourth permanent magnet of N-pole	90	°
The angle e between the first permanent magnet of S-pole	103	°
The angle g between the second permanent magnet of S-pole	92	°
The angle h between the third permanent magnet of S-pole	105	°
The angle j between the fourth permanent magnet of S-pole	92	°
The outer diameter of the rotor	59.4	mm
The outer diameter of the stator	190	mm
The inner diameter of the stator	120	mm

2.2. Simulation Verification

To verify the correctness and superiority of the bilayer segmented asymmetric V-type permanent magnet synchronous motors, the electromagnetic characteristics of interior permanent magnet synchronous motors with bilayer conventional V-type structure, bilayer segmented symmetric V-type structure, and bilayer segmented asymmetric V-type structure are simulated and analyzed. The same number of permanent magnets and same pole-arc coefficients are used in the three structures. The air-gap density, output torque, and torque ripple of the three different structures are compared to verify the feasibility of adopting the bilayer segmented asymmetric V-type structure to reduce the air-gap magnetic density distortion rate at the same time, to ensure the output torque and reduce the torque ripple. The schematic diagrams of the three different structures are shown in Fig. 2.

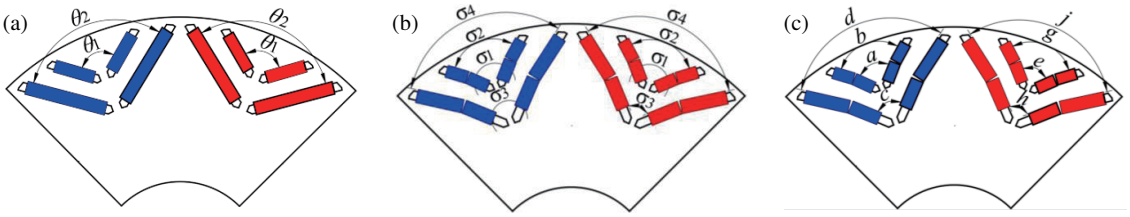

FIGURE 2. Schematic diagrams of three different structures. (a) Bilayer conventional V-type structure. (b) Bilayer segmented symmetric V-type structure. (c) Bilayer segmented asymmetric V-type structure.

The angular parameters of the three structures are shown in Table 2.

TABLE 2. Angular parameters of three structures.

Type	Parameter	Value	Unit
Bilayer conventional V-type permanent magnet	θ_1	106	°
	θ_2	106	°
Bilayer segmented symmetric V-type permanent magnet	σ_1	91	°
	σ_2	106	°
	σ_3	91	°
	σ_4	106	°
Bilayer segmented asymmetric V-type permanent magnet	a	104	°
	b	91	°
	c	106	°
	d	90	°
	e	103	°
	g	92	°
	h	105	°
	j	92	°

The comparison of the air-gap magnetic density waveforms of bilayer conventional V-type structure, bilayer segmented symmetric V-type structure, and bilayer segmented asymmetric V-type structure is shown in Fig. 3.

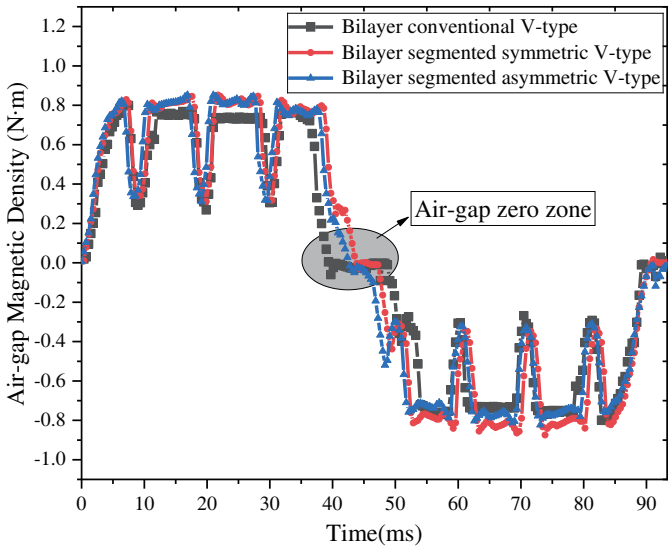

FIGURE 3. Comparison of air-gap waveforms.

The grey area in Fig. 3 shows that the air-gap magnetic density waveforms of the three structures have an air-gap magnetic density close to 0 within a certain range, and this area is defined as an "air-gap zero zone." The percentage of air-gap zero region is defined as k, which is expressed as follows:

$$k = \frac{l_{zero}}{l_{air}} \times 100\% \tag{1}$$

where l_{zero} is the length of the air-gap zero zone, and l_{air} is the length of the air-gap occupied by a pair of N-pole and S-pole.

Table 3 shows the percentages of air-gap zero region of the bilayer conventional V-type structure, bilayer segmented symmetric V-type structure, and bilayer segmented asymmetric V-type structure.

As can be seen from Table 3, the percentages of air-gap zero region of bilayer segmented symmetric V-type structure and bilayer segmented asymmetric V-type structure are much smaller than that of bilayer conventional V-type structure. Thus, the segmented structure can partially weaken the existence of the "air-gap zero zone" phenomenon. At the same time, the asymmetric structure can flexibly combine the magnetic pole angles of the N-pole and S-pole and the magnetic pole angles of the first layer and second layer to make up the air-gap zero region between the N-pole and S-pole. Thus, the bilayer segmented asymmetric V-type structure has a smaller percentage of air-gap zero region.

The comparison of air-gap density harmonic amplitude and air-gap magnetic density distortion rate for bilayer conventional V-type structure, bilayer segmented symmetric V-type structure, and bilayer segmented asymmetric V-type structure are shown in Fig. 4.

As can be seen from Fig. 3 and Fig. 4, the air-gap magnetic density peak value of the bilayer conventional V-type structure is not much different from that of the bilayer segmented symmetric V-type structure and bilayer segmented asymmetric V-type structure. However, there is an obvious concavity in the air-gap magnetic waveform of the bilayer conventional V-type structure. The bilayer conventional V-type structure has a high content of harmonics, especially 7th, 9th, 11th, 17th, 19th, etc. Hence, the air-gap magnetic density distortion rate of the bilayer conventional V-structure is high, affecting the output characteristics. The air-gap magnetic waveforms of the bilayer segmented symmetric V-structure and bilayer segmented asymmetric V-structure are close to sinusoidality, with lower high harmonics content. Thus, the air-gap magnetic density distortion rates of these two structures are smaller.

TABLE 3. Comparison of the percentages of air-gap zero region of three structures.

The percentage of air-gap zero region	Bilayer conventional V-type	Bilayer segmented symmetric V-type	Bilayer segmented asymmetric V-type
k	9.77%	5.03%	4.82%

TABLE 4. Comparison of air-gap properties of three structures.

Property	Bilayer conventional V-type	Bilayer segmented symmetric V-type	Bilayer segmented asymmetric V-type
Air-gap magnetic peak value/T	0.769	0.845	0.851
Air-gap magnetic density distortion rate	0.299	0.272	0.263

TABLE 5. Comparison of output performances of three structures.

Performance	Bilayer conventional V-type	Bilayer segmented symmetric V-type	Bilayer segmented asymmetric V-type
Maximum output torque (N·m)	15.565	16.450	16.417
Minimum output torque (N·m)	12.498	13.239	13.905
Average output torque (N·m)	13.970	14.606	14.842
Torque ripple	0.227	0.218	0.169

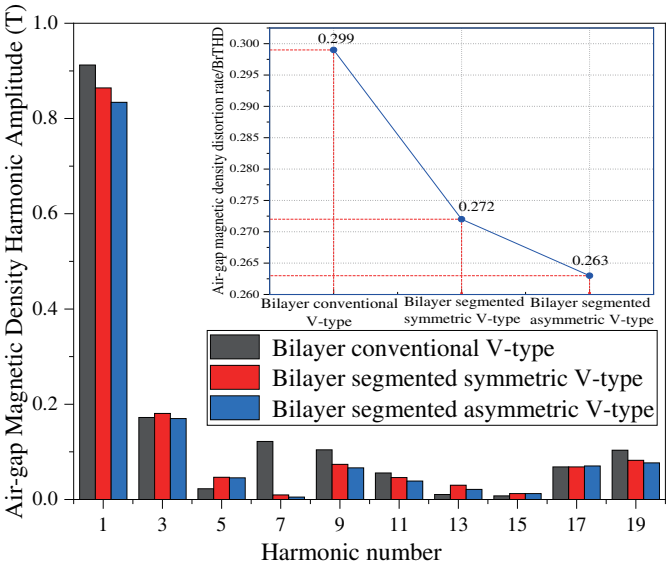

FIGURE 4. Comparison of air-gap density harmonic amplitude and air-gap density distortion rate of three structures.

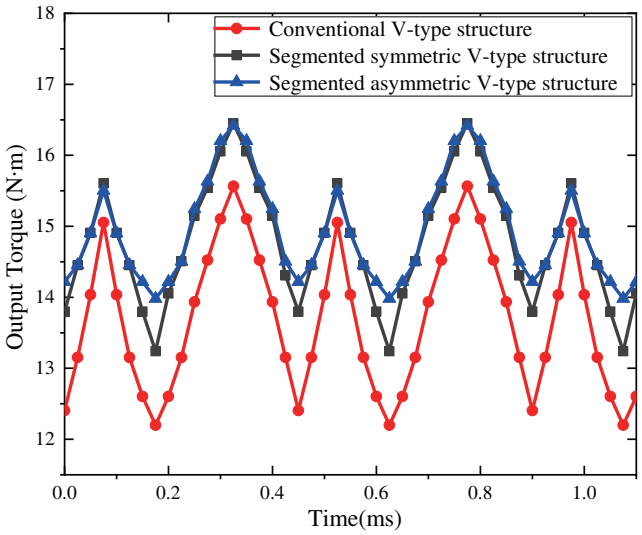

FIGURE 5. Comparison of output torques of three structures.

The comparisons of the air-gap magnetic density peak value and air-gap magnetic density distortion rate of the bilayer conventional V-type structure, bilayer segmented symmetric V-type structure, and bilayer segmented asymmetric V-type structure are shown in Table 4.

The comparisons of the output torques and torque ripples of the bilayer conventional V-type structure, bilayer segmented symmetric V-structure, and bilayer segmented asymmetric V-type structure are shown in Fig. 5 and Fig. 6.

Table 5 shows the comparison results of maximum output torque, minimum output torque, average output torque, and

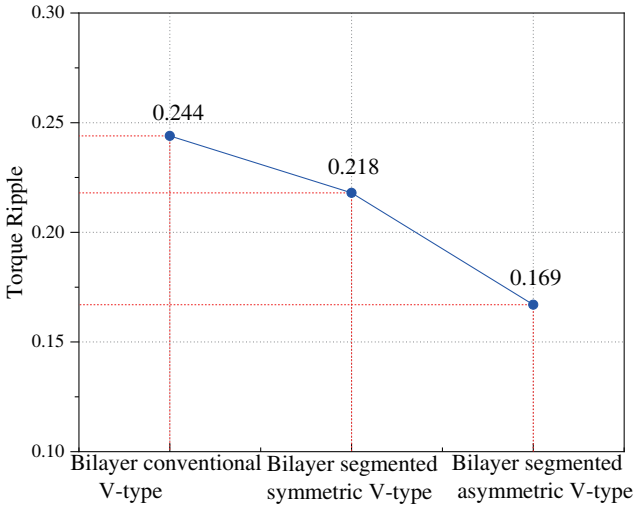

FIGURE 6. Comparison of torque ripples of three structures.

torque ripple for the bilayer conventional V-type structure, bilayer segmented symmetric V-type structure, and bilayer segmented asymmetric V-type structure.

From Table 5, it can be seen that both the bilayer segmented symmetric V-type structure and bilayer segmented asymmetric V-type structure have larger maximum output torque, minimum output torque, and average output torque, as well as smaller torque ripple than the bilayer conventional V-type structure. Meanwhile, although the maximum output torque and average output torque of the bilayer segmented asymmetric V-type structure are slightly smaller than that of the bilayer segmented symmetric V-type structure, its minimum output torque and torque ripple are better than that of the bilayer segmented symmetric V-type structure to a larger extent. It is because the segmented structure can change the pole-span angle of the inner and outer poles, and the zero region of the air gap between the N-pole and S-pole is reduced compared to bilayer conventional V-type structure, which improves the sinusoidal nature of the air-gap magnetic density waveform and thus reduces the air-gap magnetic density distortion rate. At the same time, the segmented structure can reduce magnetic leakage compared to the bilayer conventional V-type structure, so the segmented structure has higher power density and larger output torque. The presence of asymmetry in the segmented structure leads to a reduction in the harmonic content in the air-gap density, which reduces the air-gap density distortion rate and reduces the output torque ripple. Therefore, using a bilayer segmented asymmetric V-type structure can reduce the air-gap magnetic density distortion rate while improving the output performance, which includes the increase of the average output torque and the reduction of the torque ripple. The correctness of the theoretical derivation of the bilayer segmented asymmetric theory is verified.

3. ANALYTICAL MODEL

3.1. Establishment of the Analytical Model

The modeling in this paper is based on the following assumptions [20]: (1) the saturation of the stator core and rotor core except for the magnetic bridge is neglected, and the saturation at the magnetic bridge is assumed to be homogeneous; (2) the end effect is neglected; (3) the rotor magnetic potential is excited only by the permanent magnets; and (4) the motor d-axis and the axis of A-phase windings are coincident at $t = 0$.

According to the Lorentz force law, the output torque of the motor can be expressed as:

$$T_e = Lr_g \int_{2\pi} B_g dF = Lr_g \int_{2\pi} (F_r - F_s)\, \Delta_g dF \tag{2}$$

The current flowing through the stator windings of a motor produces the stator magnetic potential. It is analyzed using the winding function approach. The bilayer segmented asymmetric V-type permanent magnet bipolar model is shown in Fig. 7.

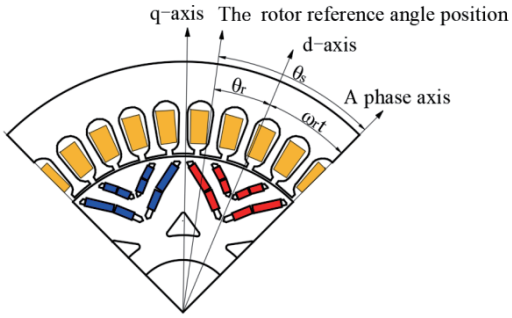

FIGURE 7. The bilayer segmented asymmetric V-type permanent magnetic bipolar model.

The winding function for each phase can be expanded in a Fourier series, as shown in (3):

$$\begin{cases} N_a(\theta_r) = \sum\limits_k N_k \cos(k\theta_r - 2\pi/3) \\ N_b(\theta_r) = \sum\limits_k N_k \cos k(\theta_r) \\ N_c(\theta_r) = \sum\limits_k N_k \cos k(\theta_r + 2\pi/3) \end{cases} \tag{3}$$

Under load conditions, the three-phase symmetrical circuit is:

$$\begin{cases} I_a(t) = I \sin(\omega_r t + \theta_0 - 2\pi/3) \\ I_b(t) = I \sin(\omega_r t + \theta_0) \\ I_c(t) = I \sin(\omega_r t + \theta_0 + 2\pi/3) \end{cases} \tag{4}$$

The stator magnetic potential generated by the current can be expressed as:

$$F_s(\theta_r, t) = N_a I_a + N_b I_b + N_c I_c \tag{5}$$

bringing (3) and (4) together gives

$$F_s(\theta_r, t) = \frac{I}{2} \sum_{i=1}^{3} \sum_{k}^{\infty} N_k \begin{Bmatrix} \sin\left[\omega_r t + k\theta_r + \theta_0 - \frac{2}{3}\pi(i-1)(1+k)\right] + \\ \sin\left[\omega_r t - k\theta_r + \theta_0 - \frac{2}{3}\pi(i-1)(1-k)\right] \end{Bmatrix} \tag{6}$$

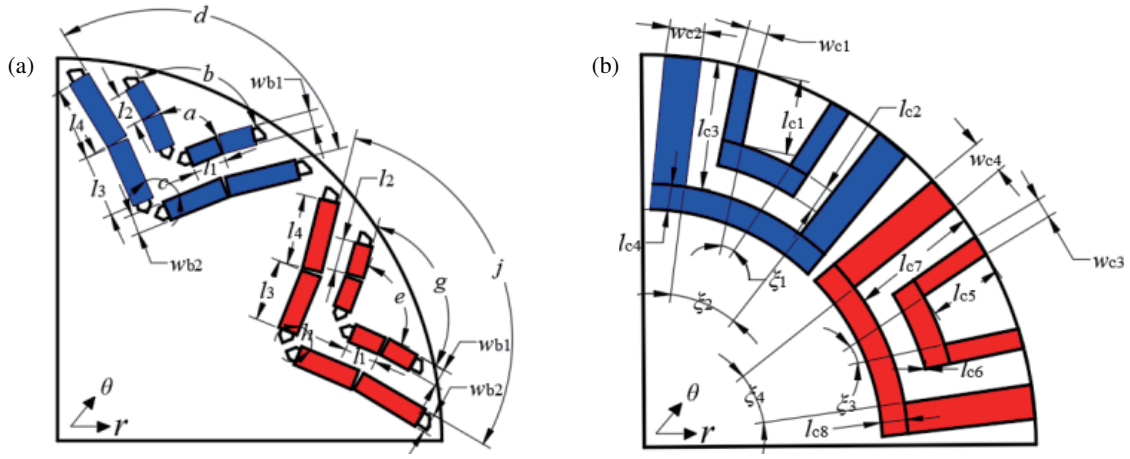

FIGURE 8. Bilayer segmented asymmetric V-type original structure and its equivalent structure. (a) Original structure. (b) Equivalent structure.

The rotor magnetic potential is calculated using the subdomain modeling method. To simplify the magnetic field's boundary conditions, the original bilayer segmented asymmetric V-type magnetic poles are replaced by an analogous structure with a combination of radial and tangential poles [21].

Figure 8 schematically shows the bilayer segmented asymmetric V-type structure and its equivalent structure, modeled in the r-θ coordinate system, with the counterclockwise direction specified as the positive direction of motor rotation.

The specific equivalent process is as follows. First of all, the equivalent structure ensures that the thickness of the permanent magnet is unchanged, and then according to the principle of the total magnetic flux remaining unchanged, the bilayer segmented asymmetric V-type permanent magnet of the N-pole can be established as:

$$\begin{cases} 2\left(l_1+l_2\right)\times w_{b1}=2l_{c1}\times w_{c1}+\dfrac{1}{2}\left(R_{N4}+R_{N3}\right) \\ \left(\xi_1+2\arctan\dfrac{w_{c1}}{R_{N4}}\right)l_{c2} \\ \xi_1=b-2\arctan\dfrac{w_{c1}}{R_{N4}} \\ R_{N4}=R_f-l_{c1} \\ R_{N3}=R_{N4}-l_{c2} \\ 2\left(l_3+l_4\right)\times w_{b2}=2l_{c3}\times w_{c2}+\dfrac{1}{2}\left(R_{N1}+R_{N2}\right) \\ \left(\xi_2+2\arctan\dfrac{w_{c2}}{R_{N2}}\right)l_{c4} \\ \xi_2=d-2\arctan\dfrac{w_{c2}}{R_{N2}} \\ R_{N2}=R_f-l_{c3} \\ R_{N1}=R_{N2}-l_{c4} \end{cases} \tag{7}$$

The bilayer segmented asymmetric V-type permanent magnet of the S-pole can be established as:

$$\begin{cases} 2\left(l_1+l_2\right)\times w_{b1}=2l_{c5}\times w_{c3}+\dfrac{1}{2}\left(R_{S3}+R_{S4}\right) \\ \left(\xi_3+2\arctan\dfrac{w_{c3}}{R_{S4}}\right)l_{c6} \\ \xi_3=g-2\arctan\dfrac{w_{c3}}{R_{S4}} \\ R_{S4}=R_f-l_{c5} \\ R_{S3}=R_{S4}-l_{c6} \\ 2\left(l_3+l_4\right)\times w_{b2}=2l_{c7}\times w_{c4}+\dfrac{1}{2}\left(R_{S2}+R_{S3}\right) \\ \left(\xi_4+2\arctan\dfrac{w_{c4}}{R_{S4}}\right)l_{c8} \\ \xi_4=e-2\arctan\dfrac{w_{c4}}{R_{S4}} \\ R_{S2}=R_f-l_{c7} \\ R_{S1}=R_{S2}-l_{c8} \end{cases} \tag{8}$$

where w_{b1} and w_{b2} are the width of the first permanent magnet and the width of the second permanent magnet, respectively; l_1 is the length of the first permanent magnet; l_2 is the length of the second permanent magnet; l_3 is the length of the third permanent magnet; l_4 is the length of the fourth permanent magnet; l_{c1} is the length of the N-pole equivalent tangential structure of the first layer; l_{c2} is the width of the N-pole equivalent radial structure of the first layer; l_{c3} is the length of the N-pole equivalent tangential structure of the second layer; l_{c4} is the width of the N-pole equivalent radial structure of the second layer; l_{c5} is the length of the S-pole equivalent tangential structure of the first layer; l_{c6} is the width of the S-pole equivalent radial structure of the first layer; l_{c7} is the length of the S-pole equivalent tangential structure of the second layer; l_{c8} is the width of the

S-pole equivalent radial structure of the second layer; a, b, c, d, e, g, h, j are magnetic pole spanning angles; ξ_1, ξ_2 are span angles between the N-pole equivalent magnetic pole tangential structures; ξ_3, ξ_4 are span angles between the S-pole equivalent magnetic pole tangential structures; R_f is the outer radius of the rotor; R_{N4} is the outer radius of N-pole equivalent radial structure of the first layer; R_{N3} is the inner radius of N-pole equivalent radial structure of the first layer; R_{N2} is the outer radius of N-pole equivalent radial structure of the second layer; R_{N1} is the inner radius of N-pole equivalent radial structure of the second layer; R_{S4} is the outer radius of S-pole equivalent radial structure of the first layer; R_{S3} is the inner radius of S-pole equivalent radial structure of the first layer; R_{S2} is the outer radius of S-pole equivalent radial structure of the second layer; R_{S1} is the inner radius of S-pole equivalent radial structure of the second layer.

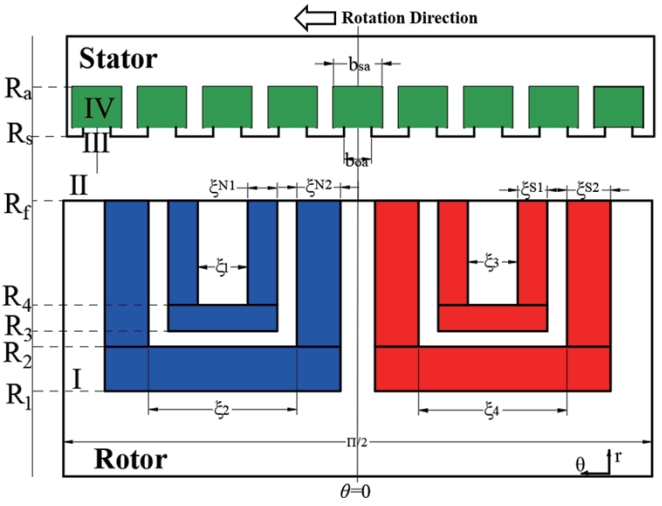

FIGURE 9. The simplified analytical calculation model.

The simplified analytical calculation model is shown in Fig. 9. In this figure, R_s is the inner radius of the stator core, R_a the radius of the stator slot bottom, and R_f the outer radius of the rotor core. The model is divided into four subdomains: rotor (I), air gap (II), stator groove (III), and stator trough (IV). The model is resolved within $\theta \in [-\pi/4, \pi/4]$, with the assumption that $\theta = 0$ at the centers of the N and S poles. The vector magnetic potential of each subdomain is satisfied:

$$\frac{\partial^2 A}{\partial r^2}+\frac{1}{r}\cdot\frac{\partial A}{\partial r}+\frac{1}{r^2}\cdot\frac{\partial^2 A}{\partial \theta^2}=-\frac{\mu_0}{r}\left(M_\theta+r\frac{\partial M_\theta}{\partial r}-\frac{\partial M_r}{\partial \theta}\right) \quad (9)$$

For the air gap subdomain, the intensity of magnetization is 0, so the subdomain satisfies:

$$\frac{\partial^2 A_\phi}{\partial r^2}+\frac{1}{r}\cdot\frac{\partial A_\phi}{\partial r}+\frac{1}{r^2}\cdot\frac{\partial^2 A_\phi}{\partial \theta^2}=0 \quad (10)$$

Taking the N-pole air gap subdomain in Fig. 9 as an example, the magnetic vector potentials of this subdomain can be expressed as:

$$\begin{aligned} A_{NII}(r,\theta) = &\sum_{n=1}\left[C_{N2n}\frac{R_f}{n}\frac{\left(\frac{r}{R_s}\right)^n+\left(\frac{R_s}{r}\right)^n}{\left(\frac{R_f}{R_s}\right)^n-\left(\frac{R_s}{R_f}\right)^n}\right. \\ &\left.+D_{N2n}\frac{R_s}{n}\frac{\left(\frac{r}{R_f}\right)^n+\left(\frac{R_f}{r}\right)^n}{\left(\frac{R_s}{R_f}\right)^n-\left(\frac{R_f}{R_s}\right)^n}\right]\cos(n\theta) \\ &+\sum_{n=1}\left[P_{N2n}\frac{R_f}{n}\frac{\left(\frac{r}{R_s}\right)^n+\left(\frac{R_s}{r}\right)^n}{\left(\frac{R_f}{R_s}\right)^n-\left(\frac{R_s}{R_f}\right)^n}\right. \\ &\left.+Q_{N2n}\frac{R_s}{n}\frac{\left(\frac{r}{R_f}\right)^n+\left(\frac{R_f}{r}\right)^n}{\left(\frac{R_s}{R_f}\right)^n-\left(\frac{R_f}{R_s}\right)^n}\right]\sin(n\theta) \\ &R_f \le r \le R_s \end{aligned} \quad (11)$$

The magnetic vector potentials $\boldsymbol{A}$ and tangential magnetic field $\boldsymbol{H}_\theta$ are continuous at the boundary of different subdomains. Thus, for the N-pole air gap subdomain, the following boundary conditions are satisfied:

$$\begin{cases} A_{NII}(R_f,\theta) = A_{N\phi}(R_f,\theta) \\ H_{NII}(R_f,\theta) = H_{N\phi}(R_f,\theta) \end{cases} \quad (12)$$

According to the boundary conditions listed in (12), combined with (11), the following can be obtained:

$$\begin{cases} C_{N2n} = \dfrac{1}{\mu_r \pi}\displaystyle\int_0^{\pi/4}\frac{\partial A_{N\phi}(r,\theta)}{\partial r}\cos(n\theta)\,d\theta \\ P_{N2n} = \dfrac{1}{\mu_r \pi}\displaystyle\int_0^{\pi/4}\frac{\partial A_{N\phi}(r,\theta)}{\partial r}\sin(n\theta)\,d\theta \\ D_{N2n} = \dfrac{1}{\pi}\displaystyle\int_0^{\pi/4}\frac{\partial A_{N\phi}(r,\theta)}{\partial r}\sin(n\theta)\,d\theta \\ Q_{N2n} = \dfrac{1}{\pi}\displaystyle\int_0^{\pi/4}\frac{\partial A_{N\phi}(r,\theta)}{\partial r}\cos(n\theta)\,d\theta \end{cases} \quad (13)$$

After solving the equations to obtain the coefficients for each subdomain, the expressions for the radial and tangential air gap magnetic flux density generated by the N-pole permanent mag-

net are obtained as follows:

$$B_{Nr}(r_g,\theta)=-\frac{1}{r_g}\begin{bmatrix}\sum\limits_{n=1}\left[C_{NIIn}R_f\dfrac{\left(\frac{r_g}{R_s}\right)^n+\left(\frac{R_s}{r_g}\right)^n}{\left(\frac{r_g}{R_s}\right)^n-\left(\frac{R_s}{r_g}\right)^n}\right.\\ \left.+D_{NIIn}R_s\dfrac{\left(\frac{r_g}{R_f}\right)^n+\left(\frac{R_f}{r_g}\right)^n}{\left(\frac{R_s}{R_f}\right)^n-\left(\frac{R_f}{R_s}\right)^n}\right]\\ \sin(n\theta)\\ -\sum\limits_{n=1}\left[P_{NIIn}R_f\dfrac{\left(\frac{r_g}{R_s}\right)^n+\left(\frac{R_s}{r_g}\right)^n}{\left(\frac{r_g}{R_s}\right)^n-\left(\frac{R_s}{r_g}\right)^n}\right.\\ \left.+Q_{NIIn}R_s\dfrac{\left(\frac{r_g}{R_f}\right)^n+\left(\frac{R_f}{r_g}\right)^n}{\left(\frac{R_s}{R_f}\right)^n-\left(\frac{R_f}{R_s}\right)^n}\right]\\ \cos(n\theta)\end{bmatrix} \tag{14}$$

$$B_{Nt}(r_g,\theta)=-\frac{1}{r_g}\begin{bmatrix}\sum\limits_{n=1}\left[C_{NIIn}R_f\dfrac{\left(\frac{r_g}{R_s}\right)^n-\left(\frac{R_s}{r_g}\right)^n}{\left(\frac{r_f}{R_s}\right)^n-\left(\frac{R_s}{r_f}\right)^n}\right.\\ \left.+D_{NIIn}R_s\dfrac{\left(\frac{r_g}{R_f}\right)^n-\left(\frac{R_f}{r_g}\right)^n}{\left(\frac{R_s}{R_f}\right)^n-\left(\frac{R_f}{R_s}\right)^n}\right]\\ \cos(n\theta)\\ +\sum\limits_{n=1}\left[P_{NIIn}R_f\dfrac{\left(\frac{r_g}{R_s}\right)^n-\left(\frac{R_s}{r_g}\right)^n}{\left(\frac{r_f}{R_s}\right)^n-\left(\frac{R_s}{r_f}\right)^n}\right.\\ \left.+Q_{NIIn}R_s\dfrac{\left(\frac{r_g}{R_f}\right)^n-\left(\frac{R_f}{r_g}\right)^n}{\left(\frac{R_s}{R_f}\right)^n-\left(\frac{R_f}{R_s}\right)^n}\right]\\ \sin(n\theta)\end{bmatrix} \tag{15}$$

The method and procedure for solving the magnetic vector potentials, as well as the boundary conditions in the subdomain of the S-pole air gap, are similar to those for the N-pole.

The rotor magnetic potential F_r can be expressed as follows:

$$F_r=\Phi_r\cdot\Delta_g=B_rA_g\frac{g}{A_g\mu_0}=B_r\frac{g}{\mu_0}$$
$$=-\frac{g}{r_g\mu_0}(M_{Nr}+M_{Sr}) \tag{16}$$

At the air gap surface, the expression for the output torque is derived from the Lorentz force law as:

$$T_e=\frac{\mu_0}{g}LR_r\int_0^{2\pi}B_gdF=\frac{\mu_0}{g}LR_r\int_0^{2\pi}(F_r-F_s)dF \tag{17}$$

The torque ripple of the motor can be expressed as:

$$T_{rip}=\frac{T_{emax}-T_{emin}}{T_{eavg}} \tag{18}$$

3.2. Validation of the Analytical Model

To verify the accuracy of the analytical model of the bilayer segmented asymmetric V-type pole structure, the air-gap magnetic density, output torque, and torque ripple calculated by the analytical model are compared with those calculated by the finite element method. The comparison results are shown in Fig. 10 and Fig. 11.

The values of the air-gap magnetic density, output torque, and torque ripple of the bilayer segmented asymmetric V-structure are compared between the analytical and simulation results, which are quite consistent. The accuracy and validity of the analytical model are verified.

4. OPTIMIZATION BASED ON SENSITIVITY HIERARCHY

According to the derivation results of Eq. (14)–Eq. (18), the motor's air-gap magnetization, output torque, and torque ripple are all related to the pole span angle of the bilayer segmented asymmetric V-type structure. Therefore, the air-gap magnetization, output torque, and torque ripple of the motor can be changed by the angles of the magnets.

In this design, the optimization variables are selected as follows: the angle a between the first permanent magnets of N-pole, the angle b between the second permanent magnets of N-pole, the angle c between the third permanent magnets of N-pole, the angle d between the fourth permanent magnets of N-pole, the angle e between the first permanent magnets of S-pole, the angle g between the second permanent magnets of S-pole, the angle h between the third permanent magnets of S-pole, and the angle j between the fourth permanent magnets of S-pole. The optimization objectives are to reduce the air-gap magnetic density distortion rate, increase the average output torque, and reduce the torque ripple. The optimization constraints for each design variable are shown in Table 6.

The optimization objective is to maximize the average output torque and minimize the torque ripple as well as the air-gap magnetic density distortion rate under the constraints, and the optimization model is:

$$\begin{cases}\max T_{avg}(x_1,x_2,\ldots,x_m)\\ \min T_{rip}(x_1,x_2,\ldots,x_m)\\ \min THD(x_1,x_2,\ldots,x_m)\end{cases} \tag{19}$$

where T_{avg} is the average output torque, T_{rip} the torque ripple, and THD the air-gap magnetic density distortion rate.

The span angles of each pole of the bilayer segmented asymmetric V-type structure are not independent, and each span angle is interconnected. At the same time, each parameter's influence on the motor's performance is complex and variable. If the parameters of each pole span angle are optimized together,

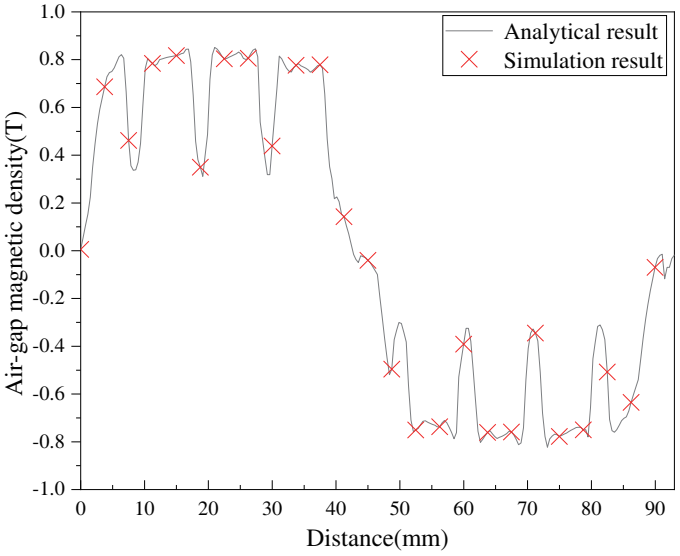

FIGURE 10. Comparison of air-gap magnetic density between the analytical result and simulation result.

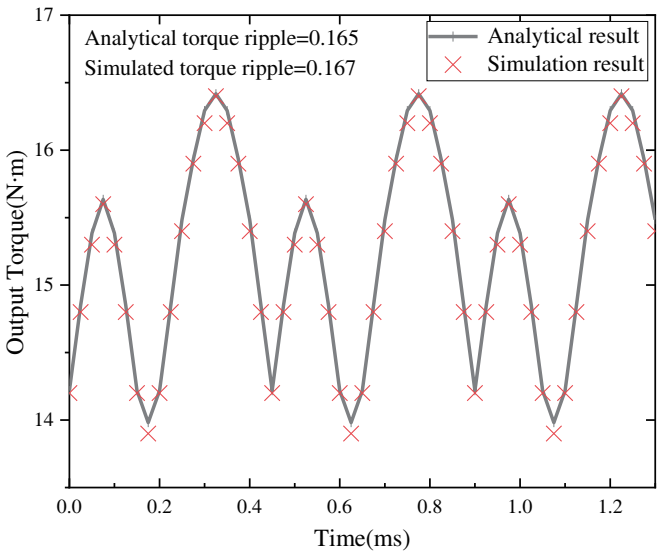

FIGURE 11. Comparison of output torque and torque ripple between the analytical result and simulation result.

TABLE 6. Comparison of air-gap properties of three structures.

Optimization variable	Sign	Initial value	Unit	Constraint
The angle between the first permanent magnets of N-pole	a	104	°	$101 \leq a \leq 109$
The angle between the second permanent magnets of N-pole	b	91	°	$88 \leq b \leq 95.5$
The angle between the third permanent magnets of N-pole	c	106	°	$104 \leq c \leq 111$
The angle between the fourth permanent magnets of N-pole	d	90	°	$88 \leq d \leq 94.5$
The angle between the first permanent magnets of S-pole	e	103	°	$103 \leq e \leq 108$
The angle between the second permanent magnets of S-pole	g	92	°	$89 \leq g \leq 96.5$
The angle between the third permanent magnets of S-pole	h	105	°	$103 \leq h \leq 110$
The angle between the fourth permanent magnets of S-pole	j	92	°	$90 \leq j \leq 96.5$

the number of test sets will increase substantially, increasing the design difficulty. Therefore, this paper adopts the sensitivity hierarchical optimization method to divide the parameters into three parts according to the sensitivity index: low-level sensitivity parameter, medium-level sensitivity parameter, and high-level sensitivity parameter.

The principle of low-level sensitivity parameter and medium-level sensitivity parameter optimization is fast but the accuracy is not required, whereas response surface optimization can clearly analyze the law of influence of two parameters on a certain optimization objective at the same time. The principle of high-level sensitivity parameter optimization is to be precise and to improve the optimization speed as much as possible. Based on Pareto frontier optimization, the relative optimal solution set can be determined under a large number of sample points, and then the optimal solution can be determined in the relative optimal solution set, which is highly accurate and fast. So, the response surface optimization is used to determine the optimal solution for low- and medium-level sensitivity parameters, and the Pareto-front solving method is used for high-sensitivity parameters to achieve multi-objective design.

The optimal parameter combination of bilayer segmented asymmetric V-type structure is obtained, and the optimized design of bilayer segmented asymmetric V-type structure permanent magnet synchronous motor is completed. The sensitivity index can be expressed by the following equation:

$$S(x_i) = AVG\left(\frac{dF(x_i)}{dx_i}\frac{x_i}{F(x_i)}\right) \tag{20}$$

where x_i is each optimization parameter of the bilayer segmented asymmetric V-type permanent magnet synchronous motor; $F(x_i)$ denotes the objective value corresponding to each optimization parameter; and AVG denotes taking the average. The size of the absolute value denotes the degree of correlation, and the positive and negative $S(x_i)$ indicate the positive and negative correlations between the optimization variables and objectives.

The sensitivity between each optimization parameter and air-gap magnetic density distortion rate, average output torque, and torque ripple is analyzed. The optimization objective sensitivity analysis is shown in Fig. 12.

Due to the uneven influence of each optimization parameter on the optimization objective, it is not possible to distin-

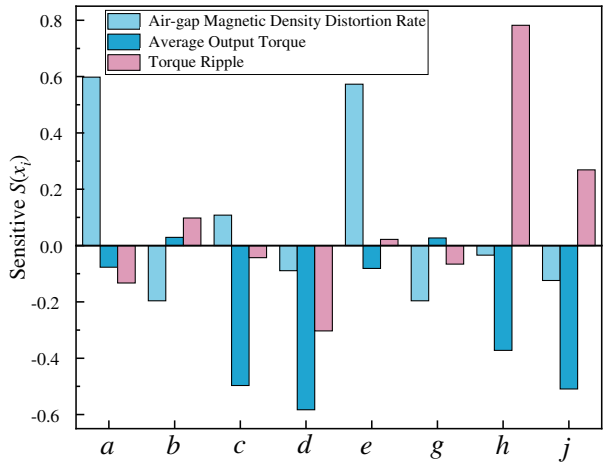

FIGURE 12. Figure of optimization objective sensitivity analysis.

guish the high-sensitivity optimization parameter from the low-sensitivity optimization parameter only by the sensitivity index of a single optimization objective. Therefore, by assigning weight coefficients to each optimization objective, a weighted sensitivity index $G(xi)$ is introduced, which can be expressed as follows:

$$G(x_i) = \lambda_A |S_A(x_i)| + \lambda_T |S_T(x_i)| + \lambda_R |S_R(x_i)| \quad (21)$$

where λ_A, λ_T, and λ_R are the weighting coefficients of the air-gap magnetic density distortion rate, average output torque, and torque ripple of the bilayer segmented asymmetric V-type permanent magnet synchronous motor, respectively; $|S_y(x_i)|$ is the absolute value of the sensitivity index of x_i to y; x_i is each optimization parameter; and y is each optimization objective.

Considering that the final performance of the motor is presented by the average output torque as well as the torque ripple, the torque ripple should be minimized as much as possible based on increasing the average output torque. In this paper, the weight λ_T of 0.5 is weighted to the average output torque, and the weight λ_R is weighted to 0.3 to the torque ripple. Since the sum of the weighting coefficients should be 1, the weight λ_A of the air-gap magnetic density distortion rate is 0.2. The weight sensitivity index for multiple optimization objectives is shown in Fig. 13.

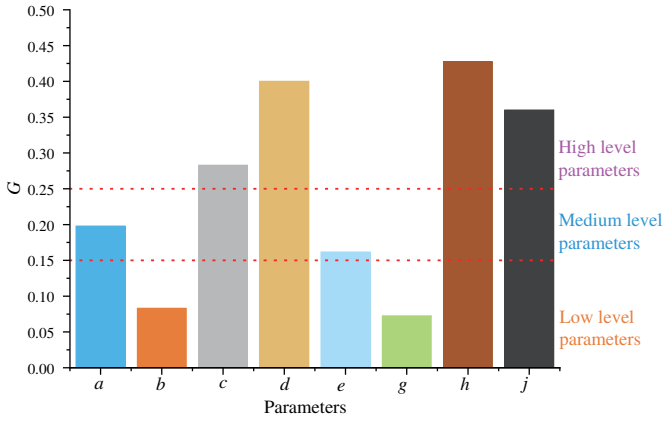

FIGURE 13. The weight sensitivity index for multiple optimization objectives.

In this paper, the optimization parameters are classified into three levels, i.e., low-level, medium-level, and high-level, as shown in Eq. (22).

$$Ranges \cong \begin{cases} \text{Low level}, & G \leq 0.15 \\ \text{Media level}, & 0.15 \leq G \leq 0.25 \\ \text{High level}, & G \geq 0.25 \end{cases} \quad (22)$$

From Fig. 13, it can be seen that the weight sensitivity of the optimization parameters b and g is less than 0.25, so the optimization parameters b and g belong to the low-level parameters. Accordingly, the optimization parameters a and e belong to the medium-level parameters, and the optimization parameters c, d, h, and j belong to the high-level parameters. Firstly, the response surface method is used to obtain the optimal values of the low-level and medium-level optimization parameters. Then, the Pareto frontier optimization method is used for the high-sensitivity parameters, and the Order Preference by Similarity to Ideal Solution (TOPIS) method is used to select the relative optimal point, and the optimal parameter combinations of the bilayer segmented asymmetric V-structure are obtained.

4.1. The Optimization of Low-Level and Medium-Level Parameters Based on the Response Surface Method

Based on the above analysis, a, b, e, and g belong to low-level and medium-level parameters, and the response surface method is used to optimize these parameters. The relationship between each parameter and the three optimization objectives is shown in Fig. 14.

Figure 14(a) shows that the air-gap magnetic distortion rate increases with a and decreases with b; the average output torque decreases with a and b; and the torque ripple does not change much with a but increases with b. Fig. 14(b) shows that the air-gap magnetic distortion rate increases with e and g; the average output torque does not change much with e and g; and the output torque ripple does not change much with e and g. Combining the above analysis, the parameter values of b, e, and g are determined to be 95.5°, 100°, and 89°, respectively. As can be seen from Fig. 13, the sensitivity of the optimization variable a on the air-gap magnetic density distortion rate is significantly higher than that of the average output torque. Therefore, priority is given to the effect of the optimization variable a on the air-gap magnetic density distortion rate, and the parameter value of a is determined as 101°.

4.2. The Optimization of Low-Level and Medium-Level Parameters Based on the Response Surface Method

The optimized low-level and medium-level parameters above are fixed, and the high-level parameters of c, d, h, and j are further optimized by using the Latin hypercube method. 100 sample points are collected for high-level parameters and response values, and some of the sample points and response values are shown in Table 7.

The actual and predicted values of the 100 sample points are counted, and the sample statistics of the optimization target points can be obtained as shown in Fig. 15. In order to evaluate the accuracy of the sample predictions, the sum of squares

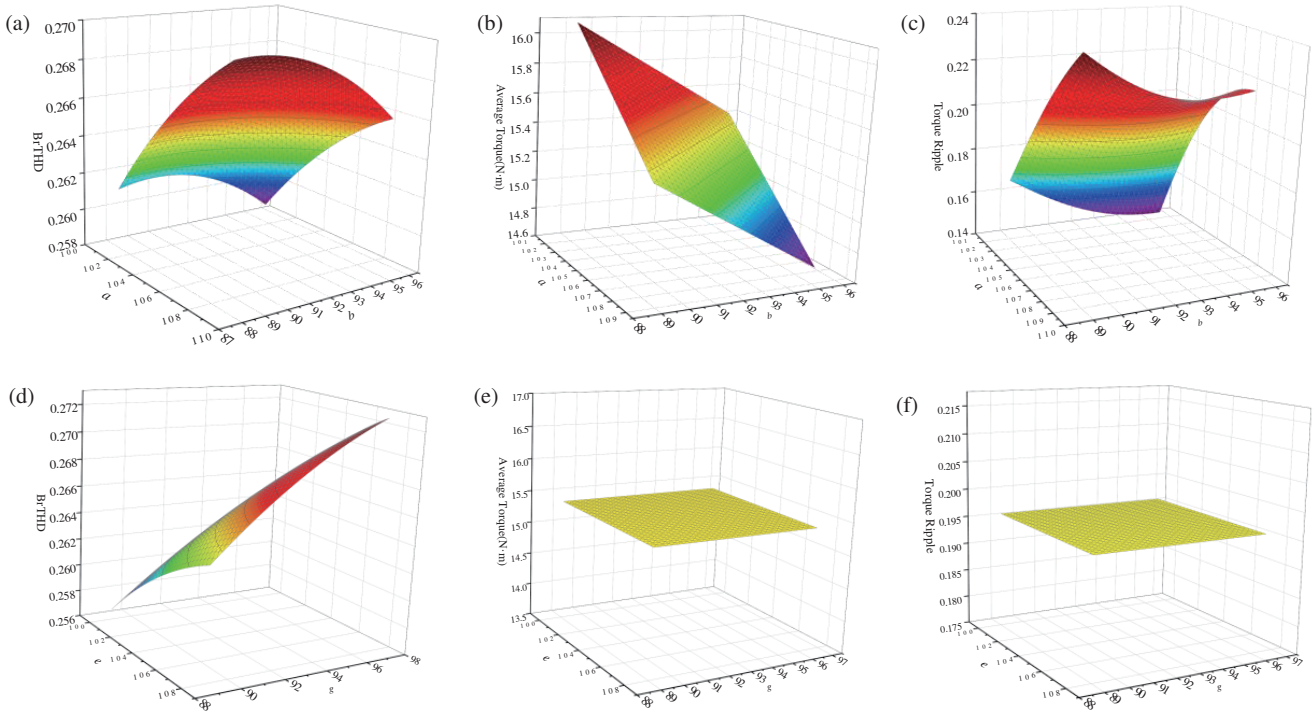

FIGURE 14. Response surface plots of low-level and medium-level parameters to the optimization objective. (a) a and b to BrTHD. (b) a and b to average torque. (c) a and b to torque ripple. (d) e and g to BrTHD. (e) e and g to average torque. (f) e and g to torque ripple.

TABLE 7. Sampling points and response values for selected design variables.

Serial number	*c*	*d*	*h*	*j*	BrTHD	T_{avg}/N·m	T_{rip}
1	109.338	91.071	103.017	92.291	0.228	15.776	0.158
2	107.798	93.834	103.542	91.901	0.235	15.426	0.157
3	108.288	91.624	103.297	92.844	0.235	15.586	0.148
4	105.172	88.504	103.367	95.606	0.234	15.672	0.182
...							
97	106.643	89.739	105.328	95.574	0.236	15.391	0.187
98	110.073	91.656	105.398	96.289	0.239	15.018	0.187
99	106.258	92.469	109.948	96.354	0.236	14.624	0.220
100	106.363	88.179	106.098	91.251	0.238	15.948	0.223

TABLE 8. Sampling points and response values for selected design variables.

Optimization objectives	Cop	Max Error	Mean Error	Root Mean Square Error
BrTHD	**0.981**	**0.007**	**0.000414**	**0.000528**
T_{avg}	**0.979**	**0.111**	**0.038124**	**0.046749**
T_{rip}	**0.963**	**0.013**	**0.003662**	**0.004550**

of the residuals and the sum of squares of the total deviations of all the samples need to be calculated, and the results of the calculations are shown in Table 8.

The root mean square error was calculated to be 0.000528, 0.046749, and 0.004550 for the three response targets, respectively. Therefore, the accuracy of the design variables in terms of changes in response values is high. At the same time, considering that 100 sample points may not be able to include all the relative best points, on this basis, using the results of 100 sample points extrapolates an additional 100 sample points, and the Pareto frontier statistics method is used for these 200 sample points. The Pareto frontier distribution is shown in Fig. 16.

As can be seen from Fig. 16, there are 64 sample points on the Pareto frontier, which are the valid values for this optimization model. The specific values of some of the Pareto frontier sample points are shown in Table 9.

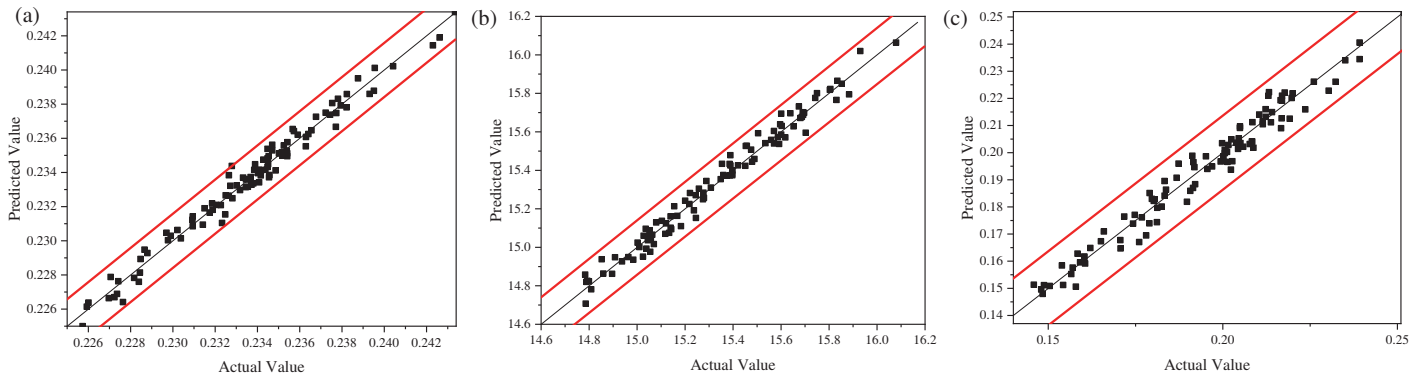

FIGURE 15. Plots of actual values versus predicted values of optimization samples. (a) Air-gap magnetic density distortion rate. (b) Output torque. (c) Torque ripple.

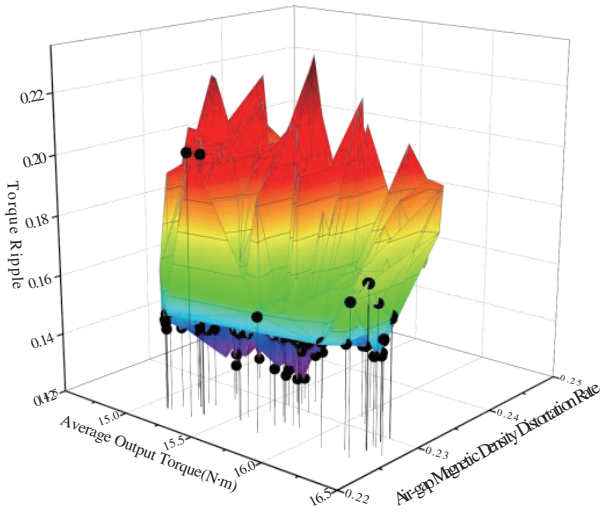

FIGURE 16. The Pareto frontier distribution.

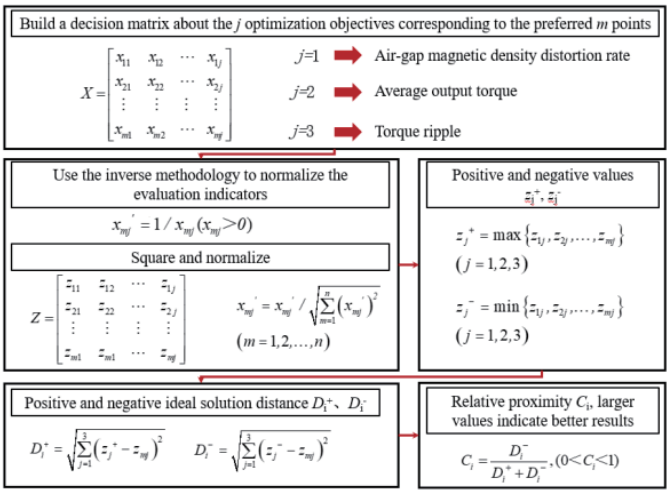

FIGURE 17. The diagram of the specific TOPIS algorithm flow.

TABLE 9. Sampling points and response values for selected design variables.

Serial number	c	d	h	j	BrTHD	T_{avg}/N·m	T_{rip}
15	107.72	91.28	103.02	91.6	0.234	15.799	0.142
23	107.72	91.28	103.02	94.15	0.228	15.589	0.147
46	107.72	91.33	103.01	91.6	0.234	15.797	0.142
58	108.12	93.44	106.61	92.08	0.224	15.339	0.205
...	...	...	...	...	...	...	...
183	−103.73	87.40	106.06	95.93	0.228	15.048	0.141
189	−103.30	92.72	107.12	90.45	0.226	16.418	0.157
193	−103.20	87.84	109.15	90.45	0.238	16.307	0.149
200	−103.3	87.83	107.76	94.65	0.227	15.858	0.150

In order to determine the relative optimal solution from the 64 Pareto frontier statistical points, the relative merits of the Pareto frontier points were evaluated using the TOPIS method. The diagram of the specific algorithm flow is shown in Fig. 17.

From the above process, the effective values of the optimization model in Table 9 are evaluated. The positive and negative ideal values of the air-gap magnetic density distortion rate, average output torque, and torque ripple are obtained as shown in Table 10.

The positive and negative ideal solution distance and relative proximity are shown in Table 11. According to the ranking results, the 189th point is chosen as the optimal solution. Thus, the high-level parameters c, d, h, and j are determined to be $-2.7°$, $2.72°$, $2.12°$, and $-1.55°$, respectively.

The results after optimization of each parameter are $a = 101°$, $b = 95.5°$, $c = 103.3°$, $d = 92.72°$, $e = 100°$, $g = 89°$, $h = 107.12°$, and $j = 90.45°$, respectively. Correspondingly, the values of the optimized air-gap magnetic density distor-

TABLE 10. The positive and negative ideal values for the three optimization objectives.

Optimization objective	Positive ideal values $z+$	Negative ideal values $z-$
Air-gap magnetic density distortion rate	0.264	0.253
Output Torque	16.328	15.048
Torque ripple	0.206	0.127

TABLE 11. The positive and negative ideal solution distances and relative proximity for the three optimization objectives.

Serial number	The positive ideal solution distance $D+$	The negative ideal solution distance $D-$	Relative proximity C	Order
15	0.533	0.751	0.585	21
23	0.741	0.542	0.422	37
46	0.535	0.749	0.583	22
58	0.990	0.301	0.233	43
...	...	...	...	...
183	1.282	0.016	0.012	64
189	0.035	1.271	0.973	1
193	0.062	1.259	0.953	9
200	0.473	0.811	0.631	19

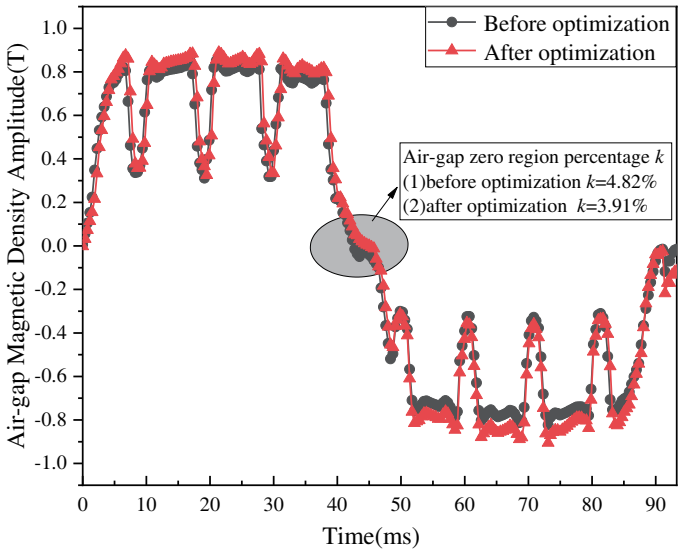

FIGURE 18. Comparison of air-gap magnetic density waveforms before and after optimization.

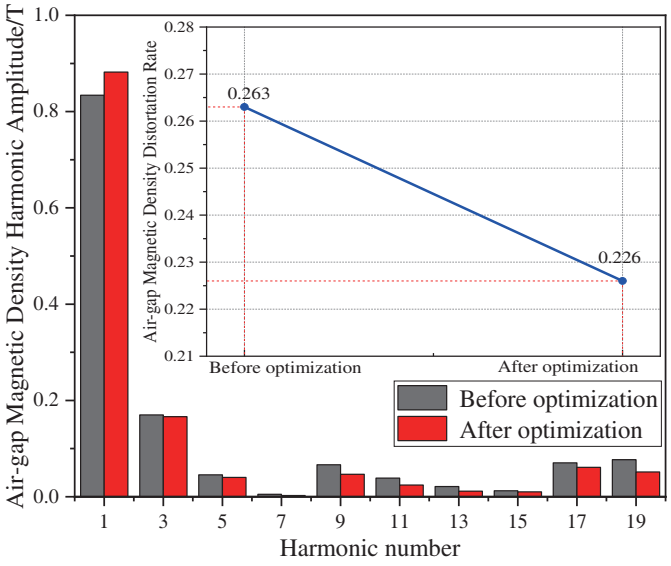

FIGURE 19. Comparison of air-gap density harmonic amplitude and air-gap magnetic density distortion rate before and after optimization.

tion rate, average output torque, and torque ripple are 0.226, 16.418 N·m, and 0.157, respectively.

5. VALIDATION OF OPTIMIZATION RESULTS

5.1. Finite Element Validation

Due to the fact in practice, the high accuracy of the magnetic pole span angle can lead to machining difficulties and errors. The values of the combined parameters of the optimized bi-layer segmented asymmetric V-type structure are now rounded to obtain $a = 101°$, $b = 95.5°$, $c = 103.3°$, $d = 92.7°$, $e = 100°$, $g = 89°$, $h = 107.1°$, and $j = 90.5°$. The optimized and rounded bilayer segmented asymmetric V-type permanent magnet synchronous motor is simulated and compared with the pre-optimization one. The comparisons of the air-gap magnetic density distortion rate, output torque, and torque ripple before and after the optimization are shown in Fig. 18, Fig. 19, and Fig. 20.

The comparison results of air-gap density peak value, air-gap magnetic density distortion rate, the percentage of air-gap zero region, maximum output torque, minimum output torque,

TABLE 12. Comparison of each performance before and after optimization.

Performance	Before optimization	After optimization	Extent
Air-gap density peak value	0.852	0.887	Increased by 4.1%
Air-gap magnetic density distortion rate	0.263	0.226	Decreased by 14.1%
Percentage of air-gap zero region	4.82%	3.91%	Decreased by 18.8 %
Maximum output torque (N·m)	16.417	17.420	Increased by 6.1%
Minimum output torque (N·m)	13.905	14.857	Increased by 6.8%
Average output torque (N·m)	14.842	16.418	Increased by 10.6%
Torque ripple	0.169	0.156	Decreased by 7.7%

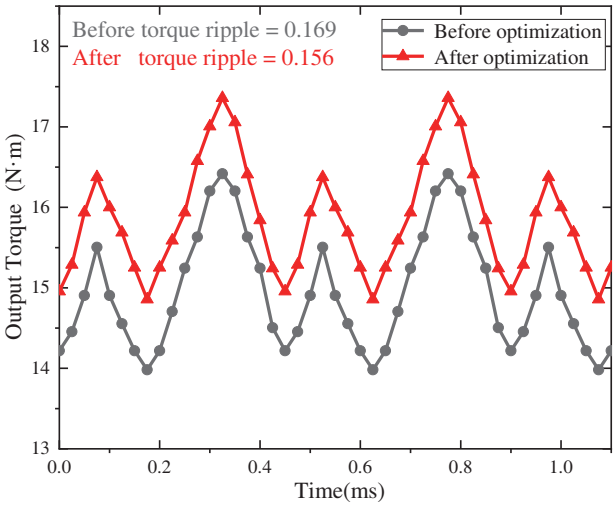

FIGURE 20. Comparison of output torque and torque ripple before and after optimization.

average output torque, and torque ripple before and after optimization are shown in Table 12.

As can be seen from Table 12, the air-gap density peak value, air-gap magnetic density distortion rate, the percentage of air-gap zero region, maximum output torque, minimum output torque, average output torque, and torque ripple are all improved to different degrees. Among them, the air-gap magnetic density distortion rate is reduced from 0.263 to 0.226, which is decreased by 14.1%; the average output torque is increased from 14.842 N·m to 16.418 N·m, which is increased by 10.6%; and the torque ripple is reduced from 0.169 to 0.157, which is decreased by 7.7%. The effectiveness of the above optimization process is verified.

5.2. Experimental Verification

In order to verify the correctness of the theoretical analysis and the effectiveness of the optimized design in this paper, a test prototype was fabricated according to the optimized design results, as shown in Fig. 21.

The air-gap magnetic density distortion rate cannot be proved by test equipment at present, but it can be proved indirectly with the no-load back electromotive force. The no-load back electromotive force is generated from the permanent magnets cutting the magnetic field when the motor is rotating. It can be shown that the air-gap magnetic field can affect the no-load back electromotive force. Therefore, the air-gap magnetization of the prototype can be indirectly reflected by measuring the no-load back electromotive force of the prototype.

The no-load back electromotive force tester and dynamometer test bench are shown in Fig. 22 and Fig. 23. The no-load back electromotive force tester is mainly composed of a controller, a prototype, coupling, a dynamometer, and a console. The dynamometer test bench is mainly composed of a dynamometer, a torque transducer, a prototype, and a controller. The most important part, controller, is mainly composed of main control board (control core for motor controllers), driver board (mainly used to control drive and protect IGBT normal operation), Insulated-Gate Bipolar Transistor (IGBT), current sensor, support capacitor, passive discharge resistor, copper row, heat sink, shell, connectors, wiring harness, and other parts.

The no-load reverse electromotive force is tested by the reverse drag method, using the prime mover to drag the test motor, doing no-load generator operation at synchronous speed, determining the three line voltages at the output of the test machine, and taking the average value of them as the no-load reverse electromotive force. The results of the no-load back electromotive force test are shown in Fig. 24. From Figure 24, the peak value of the no-load back electromotive force is 41.5 V. The waveform of the no-load back electromotive force is close to sinusoidality. It can be indirectly proved that the air-gap magnetization waveform of the prototype is close to sinusoidality. Thus, it is verified that the bilayer segmented asymmetric V-type structure can reduce the air-gap magnetic density distortion rate.

The output torque and torque ripple are measured by dynamic method. The output torque is converted into an electric signal by a torque sensor under the motor running state, and then the motor output torque value is obtained by a signal processing circuit. The torque ripple is calculated by the output torque value. The comparisons between the output torque and torque ripple test results and the simulation results are shown in Fig. 25.

The results of the comparison between test and simulation regarding average output torque and torque ripple are shown in Table 13.

As can be seen from Table 13, the relative errors of both the test and simulation results are small. The relative errors between the average output torque and torque ripple simula-

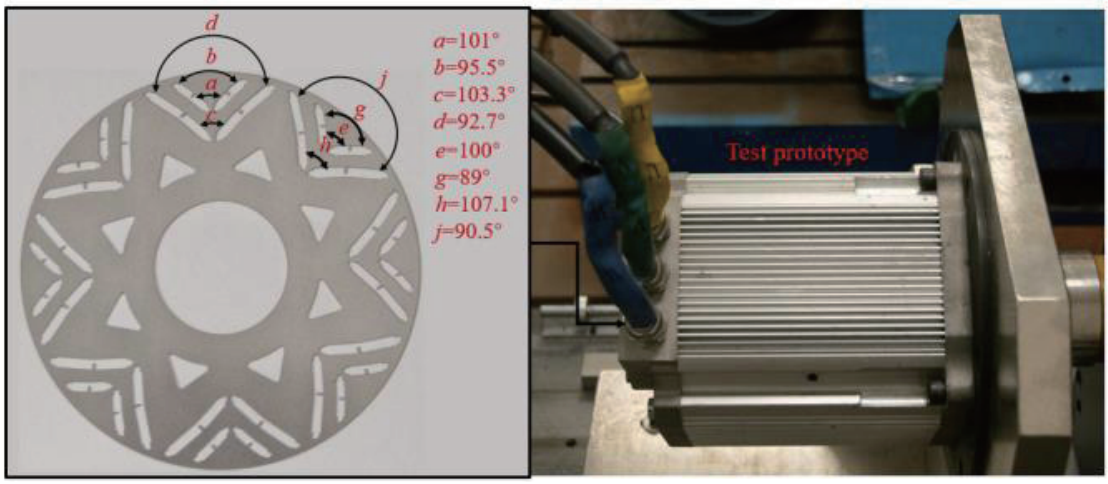

FIGURE 21. Test prototype.

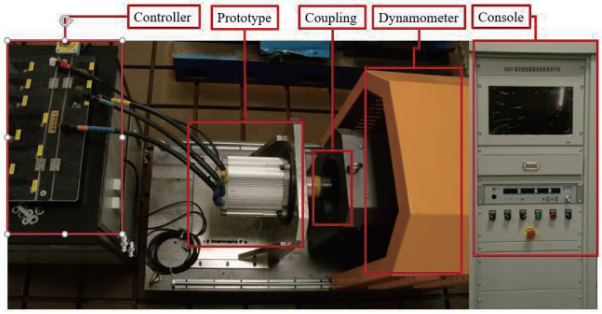

FIGURE 22. The no-load back electromotive force tester.

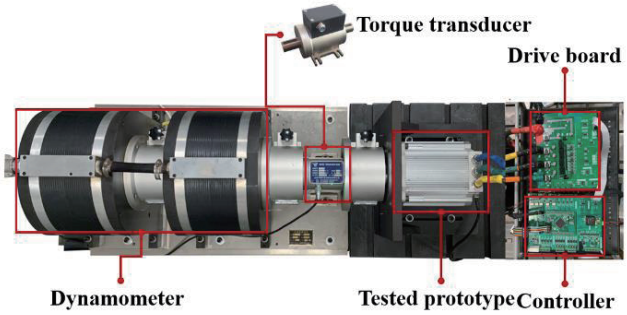

FIGURE 23. Dynamometer test bench.

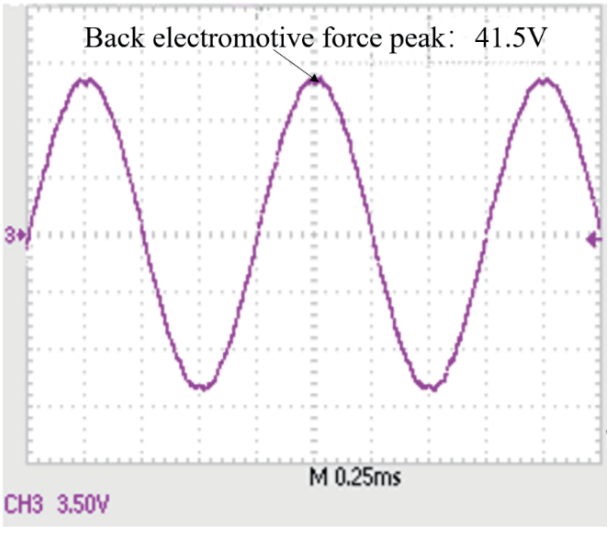

FIGURE 24. No-load back electromotive force test results.

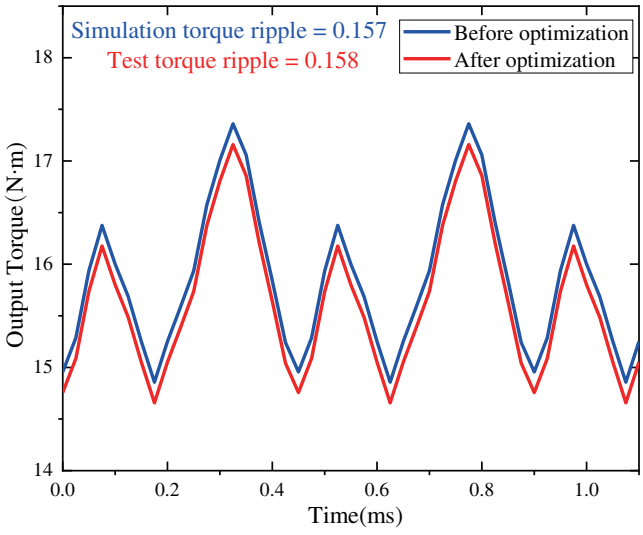

FIGURE 25. Comparison of output torque test and simulation results.

tion values and test values are 0.38% and 0.63%, respectively, which meet the design requirements. The relative error between the test results and the simulation results is because the ideal finite element model cannot take into account the machining error of the prototype and the mechanical friction of the test platform. The tests show that the bilayer segmented asymmetric V-type structure can ensure the average output torque while reducing the torque ripple.

TABLE 13. Comparison of between test and simulation results.

Output performance	Test result	Simulation result	Relative error
Average output torque (N·m)	16.257	16.318	0.38%
Torque ripple	0.158	0.157	0.63%

6. CONCLUSION

In this paper, a bilayer segmented asymmetric V-type structure permanent magnet synchronous motor is proposed. The stator magnetic potential and rotor magnetic potential are modeled and analyzed by the winding function method and subdomain model method, respectively. The analytical equation of the bilayer segmented asymmetric V-type structure on the magnetic density distortion rate, output torque, and torque ripple on the pole span angle are deduced, and finite-element simulation is used to verify the correctness of the theoretical derivation. The sensitivity stratification method is adopted to classify the optimization parameters into low-level, medium-level, and high-level parameters. The response surface optimization method is adopted for the low-level and medium-level sensitivity parameters, and the Pareto frontier optimization level is adopted for the high-level parameters. The relative optimal solution set is determined according to the Pareto frontier distribution, and the optimal span angle combination of the motor is determined by TOPIS in the relative optimal solution set. The performance parameters of the motor before and after optimization are compared by finite element simulation, and the comparison results show that the air-gap magnetic density distortion rate is reduced by 14.1%, the percentage of air-gap zero region reduced by 18.8%, the average output torque improved by 10.6%, and the torque ripple reduced by 7.7%. The optimization objectives are all improved. Finally, the prototype is fabricated and tested, and the test results are basically consistent with the simulation ones. The results show that a bilayer segmented asymmetric V-type structure proposed in this paper has a smaller air-gap magnetic density distortion rate and a percentage of air-gap zero region, as well as a larger average output torque and a smaller torque ripple, which verifies the correctness of the above theoretical analysis and the validity of the optimized design. In the future, this structure can be used in electric vehicles due to its superior advantages with a smaller air-gap magnetic density distortion rate, a larger average output torque, and a smaller torque ripple. The multi-objective optimization method proposed in this paper can be used as a new optimization idea. However, this paper still have a limitation, i.e., the analytical model does not consider saturation in the stator and rotor core due to magnet flux. This limits the applicability of the analytical model to estimate torque under load with heavy saturation. It will be the future research direction.

ACKNOWLEDGEMENT

This work was supported in part by the National Natural Science Foundation of China under Grant 52275261 and Grant 52305267 and in part by the Natural Science Foundation of Shandong Province of China Grant ZR2023QE010.

REFERENCES

[1] Cheng, M., P. Han, and W. Hua, "General airgap field modulation theory for electrical machines," *IEEE Transactions on Industrial Electronics*, Vol. 64, No. 8, 6063–6074, Aug. 2017.

[2] Son, J.-C., J.-Y. Kim, J.-W. Choi, D.-K. Lim, and H.-K. Yeo, "Performance enhancement of the IPMSM for HEV applications using grain-oriented electrical steel and design optimization," *IEEE Access*, Vol. 10, 46 599–46 607, 2022.

[3] Zhang, X., Q. Du, S. Ma, H. Geng, W. Hu, Z. Li, and G. Liu, "Permeance analysis and calculation of the double-radial rare-earth permanent magnet voltage-stabilizing generation device," *IEEE Access*, Vol. 6, 23 939–23 947, 2018.

[4] Liang, J., D. Liu, Y. Gao, H. Yuan, and X. Liu, "Design and analysis of a novel mechanical variable flux interior permanent magnet synchronous motor," *Progress In Electromagnetics Research C*, Vol. 123, 167–179, 2022.

[5] Ghadamyari, M. A., M. Moallem, and B. Fahimi, "Improving the torque characteristics of interior PM synchronous motor using an asymmetric on-off method on the rotor surface," *Progress In Electromagnetics Research M*, Vol. 54, 55–65, 2017.

[6] Kim, H., Y. Park, S.-T. Oh, C.-S. Jin, J. Lee, and W.-H. Kim, "Study on the design of six-phase surface inset permanent magnet synchronous generator and motor considering the power factor and torque ripple," *IEEE Transactions on Magnetics*, Vol. 58, No. 2, 1–5, Feb. 2022.

[7] Qu, G., Y. Fan, and Q. Chen, "Suppression of torque ripple in a new consequent-pole permanent magnet machine by segmented structure," *IEEE Transactions on Magnetics*, Vol. 58, No. 8, 1–6, Aug. 2022.

[8] Wang, S., Y. Wang, C. Liu, G. Lei, J. Zhu, and Y. Guo, "Detent force minimization of a tubular flux-switching permanent magnet motor using un-equal width stator slots based on taguchi method," *IEEE Transactions on Applied Superconductivity*, Vol. 30, No. 4, 1–5, Jun. 2020.

[9] Ma, P., Q. Wang, Y. Li, S. Jiang, and M. Zhao, "Research on torque ripple suppression of the slotted limited angle torque motor," *IEEE Transactions on Magnetics*, Vol. 57, No. 2, 1–6, Feb. 2021.

[10] Hu, P., D. Wang, *et al.*, "Sinusoidal optimization model for air gap magnetic field of eccentric magnetic pole permanent magnet motor," *Transactions of China Electrotechnical Society*, Vol. 34, No. 18, 3759–3768, Sep. 2019.

[11] Qi, X., F. Gao, *et al.*, "Optimal design of new eccentric magnet pole for surface mounted permanent magnet synchronous motors," *Journal of Electronic Measurement and Instrumentation*, Vol. 34, No. 8, 93–100, Aug. 2020.

[12] XU, Y., Q. Li, and T. Wang, "Optimal design of no-load airgap flux density of permanent magnet synchronous motor," *Journal of Southwest Jiaotong University*, Vol. 22, No. 4, 513–516, 2009.

[13] Ma, P., Q. Wang, Y. Li, S. Jiang, and M. Zhao, "Research on torque ripple suppression of the slotted limited angle torque motor," *IEEE Transactions on Magnetics*, Vol. 57, No. 2, 1–6, Feb. 2021.

[14] Park, J.-C., J.-H. Kim, S.-H. Park, K.-O. Kim, M.-H. Sung, and M.-S. Lim, "Design optimization using asymmetric rotor in IPMSM for torque ripple reduction considering forward and reverse directions," *IEEE Transactions on Magnetics*, Vol. 59, No. 11, 1–5, Nov. 2023.

[15] Ren, W., Q. Xu, Q. Li, and L. Zhou, "Reduction of cogging torque and torque ripple in interior PM machines with asymmetrical V-type rotor design," *IEEE Transactions on Magnetics*, Vol. 52, No. 7, 1–5, Jul. 2016.

[16] Xiao, Y., Z. Q. Zhu, G. W. Jewell, J. T. Chen, D. Wu, and L. M. Gong, "A novel asymmetric interior permanent magnet synchronous machine," *IEEE Transactions on Industry Applications*, Vol. 58, No. 3, 3370–3382, 2022.

[17] Muhammad, N., F. Khan, B. Ullah, and B. Alghamdi, "Performance analysis and design optimization of asymmetric interior permanent magnet synchronous machine for electric vehicles applications," *IET Electric Power Applications*, Vol. 18, No. 4, 425–435, 2024.

[18] Ge, Y., H. Yang, W. Wang, H. Lin, and Y. Li, "A novel interior permanent magnet machine with magnet axis shifted effect for electric vehicle applications," *World Electric Vehicle Journal*, Vol. 12, No. 4, 189, 2021.

[19] Ding, F., L. Shi, *et al.*, "Hybrid algorithm optimization design of segmented permanent magnet synchronous motor," *Machine Tool & Hydraulics*, Vol. 51, No. 4, 23–29, 2023.

[20] Liu, W., H. Yang, H. Lin, F. Peng, S. Lyu, and X. Huang, "Thermal modeling and analysis of hybrid-magnetic-circuit variable flux memory machine," *IEEE Transactions on Industry Applications*, Vol. 59, No. 2, 1307–1318, Mar.-Apr. 2023.

[21] Li, S., W. Tong, M. Hou, S. Wu, and R. Tang, "Analytical model for no-load electromagnetic performance prediction of V-shape IPM motors considering nonlinearity of magnetic bridges," *IEEE Transactions on Energy Conversion*, Vol. 37, No. 2, 901–911, Jun. 2022.